catalysts

MDPI

Article

Electrochemically Synthesized Fe–Mn Mesh Catalysts for Catalytic Ozonation Degradation of Phenol

Fengyin Sun [1,†], Haoyuan Gu [1,†], Jing Wang [1], Jing Xu [1,2,*] and Minghui Zhu [1,*]

[1] State Key Laboratory of Green Chemical Engineering and Industrial Catalysis, School of Chemical Engineering, East China University of Science and Technology, Shanghai 200237, China
[2] University Engineering Research Center of Green Chemical New Materials, School of Chemistry and Chemical Engineering, Guangxi University, Nanning 530004, China
* Correspondence: xujing@ecust.edu.cn (J.X.); minghuizhu@ecust.edu.cn (M.Z.)
† These authors contributed equally to this work.

Abstract

Supported catalysts for liquid-phase catalytic ozonation often suffer from active-species detachment under ozone-bubble shear and continuous-flow operation, limiting long-term stability and causing persistent metal leaching. Herein, Mn-doped iron-mesh catalysts (*x*-FMM, x = 0.04, 0.08, 0.12) were synthesized via a modified cyclic chronopotentiometry method, and their catalytic performance and ozone-activation behavior in the ozonation of phenol were systematically investigated. XRD, SEM, and BET analyses revealed that Mn incorporation reduced the Fe_2O_3 crystallite size and produced a denser, more uniform granular morphology, thereby increasing the density of accessible surface hydroxyl active sites. Quasi in situ XPS, DMPO spin-trapping EPR, before/after-reaction ATR-FTIR, ozone-decomposition, and radical-quenching experiments jointly support a radical-mediated pathway in which hydroxyl/water-related surface species participate in ozone activation and HO· generation, while Fe–Mn electronic interaction is consistent with facilitated Fe^{2+} regeneration and sustained catalytic turnover. Under optimized electrodeposition conditions, 0.08FMM achieved 87.8% phenol removal and 60.5% TOC removal after 30 min at 25 °C. During a 20 h continuous-flow test, phenol removal decreased to ~82% within the initial 2 h and then remained near 79–80%, while Fe and Mn leaching decreased to ~4–5 and ~1–2 μg L^{-1}, respectively, by 20 h. The electrochemical approach therefore provides a direct anchoring route for structured heterogeneous catalytic ozonation without high-temperature calcination, with moderate activity retention and low metal leaching under extended operation.

Keywords: catalytic ozonation; Fe–Mn mesh catalyst; electrochemical synthesis; phenol degradation; hydroxyl radical

Check for updates

Academic Editor: Gassan Hodaifa

Received: 9 September 2026
Revised: 29 September 2026
Accepted: 2 October 2026
Published: 20 October 2026

Copyright: © 2026 by the authors. Licensee MDPI, Basel, Switzerland. This article is an open access article distributed under the terms and conditions of the Creative Commons Attribution (CC BY) license.

1. Introduction

Catalytic ozonation is a highly efficient water-treatment technology that removes refractory organic pollutants through reactive oxygen species (ROS), especially hydroxyl radicals (HO·), which are strongly oxidizing and non-selective [1]. The technology has been widely applied to the degradation of organic pollutants and to water purification. However, the reactivity of ozone is strongly influenced by reaction conditions and by the catalyst; the introduction of a catalyst can markedly improve ozone utilization and reaction efficiency, and catalyst stability and activity are especially critical in heterogeneous systems.

Structured catalysts with mesh, foam, or monolithic architectures have recently emerged as attractive alternatives to conventional particulate catalysts, offering lower pressure drop, improved heat and mass transfer, and superior mechanical stability [2,3]. In the context of water treatment, Wang et al. fabricated a Cu_2O–CuO/Cu structured catalyst by in situ thermal oxidation–reduction of copper foam and achieved 94–100% ozone conversion at high space velocities [4], highlighting the promise of structured architectures for catalytic ozonation.

For water-treatment applications, iron-based materials are attractive heterogeneous catalytic supports owing to their high activity, low cost, low toxicity, and ease of recovery, and can effectively degrade phenols, pesticides, and antibiotics [5,6]. However, the limited number of surface active sites restricts ozone-decomposition efficiency and pollutant oxidation, particularly for high-concentration or recalcitrant pollutants [7]. To overcome this bottleneck, various modification strategies—such as metal doping, surface modification, and polymerization—have been explored. Metal doping, in particular, can optimize the electronic structure of the catalyst and introduce additional surface active sites, thereby markedly enhancing catalytic efficiency [8]; it also accelerates electron migration between transition metals and the generation of active radicals, thereby further improving catalytic efficiency [9]. Manganese, an earth-abundant transition metal with multiple oxidation states, can efficiently participate in electron-transfer processes during catalytic reactions and is therefore a promising dopant for modifying iron-based catalysts [10].

Supported metal catalysts are widely used in catalytic ozonation because of their easy recovery, reusability, and high dispersion of active components. However, most of these catalysts are prepared by impregnation or hydrothermal methods, which are complex and costly; for instance, Cai et al. prepared Mn–Co@Fe mesh catalysts through hydrothermal growth of precursor hydroxides followed by calcination [11]; although effective, such processes require multi-step high-temperature treatment, and the active species can detach under the impact of bubbles and fluid flow during reaction [11,12]. Electrochemical deposition is a convenient method for preparing highly stable catalytic materials: the resulting coatings adhere strongly to the substrate, enabling robust anchoring of active components on the support surface and effectively preventing detachment [13]. Representative examples include Verlato et al., who electrochemically deposited CeO_2–Pt layers on Fe–Cr–Al alloy foams for low-temperature methanol combustion [14], and Ho et al., who used single-step cathodic electrodeposition to prepare Pd–CeO_2 coatings on Fe-Cr alloy foams with strong adhesion and stable catalytic activity for CO oxidation [15]. These studies demonstrate the versatility of electrochemical synthesis for structured catalysts in both gas-phase and liquid-phase reactions. Building on this method, our group previously established single-step electrochemical synthesis of structured Cu mesh catalysts [13] and demonstrated Mn-doping control of their surface activity [16]; a recent patent application (CN121755204A, published 31 March 2026) has also disclosed the broader concept of electrochemically preparing Fe-based monolithic mesh catalysts, including Mn-containing systems for phenol ozonation [17]. Accordingly, the present study does not claim novelty for the electrochemical preparation concept itself; instead, it focuses on controlled Mn modification of the electrochemically formed Fe-based surface layer and its structure–performance relationships in liquid-phase ozonation. Recent literature on Mn–Fe heterogeneous catalytic ozonation further contextualizes this gap: Wu et al. [18] reported $MnFe_2O_4$/MoS_2 powders that enhanced phenol degradation by ~20% (200 mg L^{-1} phenol) but were prepared via hydrothermal routes; Dai et al. [19] loaded Fe–Mn onto a Ni-induced graphitized carbon–Al_2O_3 framework (Fe-Mn/NiCAF) for paint wastewater treatment; and He et al. [20] developed a Mn–Ce dual single-atom catalyst that synergistically triggers ROS generation for ozonation of emerging contaminants. Dual-site Mn–Fe approaches combining MnN_3

single-atoms with Fe_1@FeN_4 atomic clusters [21] further extend activity and stability, but rely on ZIF-derived N-doped carbon supports prepared via high-temperature pyrolysis. Against this backdrop, the differentiator of the present work is not catalytic activity per se—the phenol removal of 87.8% at 300 mg L^{-1} phenol is comparable to Cai's Mn–Co@Fe mesh and Zhang's Mn–Fe MOF [22]—but the systematic correlation of controlled Mn modification of the electrochemically formed Fe-based surface layer with catalyst structure, surface chemistry, catalytic activity, and cycling behavior, together with the absence of high-temperature calcination.

On this basis, the present work focuses on the catalytic ozonation of phenol and systematically investigates the performance, structure, and reaction mechanism of structured Fe–Mn mesh catalysts prepared by cyclic chronopotentiometry. The effects of Mn doping on catalyst structure and morphology were probed by XRD, SEM, and related techniques, while the ozone-activation behavior and the role of the catalyst were investigated using quasi in situ XPS, ozone-decomposition and radical-quenching experiments, DMPO spin-trapping EPR, and before/after-reaction ATR-FTIR. Conventional powder or particulate ozonation catalysts suffer from particle attrition, bed-pressure rise, and catalyst loss in fixed-bed or fluidised reactors, while mesh-supported catalysts produced by impregnation or hydrothermal routes still risk active-species detachment under the impact of ozone bubbles and continuous water flow. Cyclic chronopotentiometry anchors the Mn-doped Fe (hydr)oxide active layer directly onto a metal mesh through a single electrochemical anchoring step, simultaneously addressing active-site abundance and mechanical stability.

2. Results and Discussion

2.1. Catalytic Ozonation Performance

The phenol and TOC removal efficiencies after 30 min of reaction over the different catalysts are shown in Figure 1. In the absence of a catalyst, phenol removal was only 48%; adding FM noticeably enhanced the removal, and 0.08FMM gave the highest phenol removal (77.3%) under these preliminary electrodeposition conditions. Notably, 0.04FMM (75.9%) and 0.08FMM (77.3%) showed similar phenol removal under these preliminary conditions; 0.08FMM was therefore selected as the representative composition for subsequent characterization rather than as the unique "optimum" based on this screening alone. Here, the *x*-FMM labels refer to nominal $Mn(NO_3)_2$ electrolyte concentrations rather than actual Mn contents; ICP-OES measured 8.51, 14.24, and 11.28 wt% Mn for 0.04FMM, 0.08FMM, and 0.12FMM, respectively (Table S1). Because the Fe content increased monotonically over the same series, the lower Mn fraction in 0.12FMM is tentatively attributed to reduced Mn-deposition efficiency at the highest $Mn(NO_3)_2$ concentration rather than simple bulk deposit detachment (Section S1). The TOC removal followed the same trend, with 0.08FMM giving the highest TOC removal (51.4%) and the ozone-alone system giving the lowest (22.6%). The corresponding TOC removals over FM, 0.04FMM, and 0.12FMM were 38.7%, 47.1%, and 45.9%, respectively. TOC removal was consistently lower than phenol removal across all systems, indicating that some intermediates from phenol degradation were not fully mineralized. Accordingly, phenol disappearance is not treated as equivalent to complete mineralization, and the mechanistic discussion below is limited to ozone activation and reactive-species generation rather than a complete molecular transformation pathway. To verify that this activity reflects catalytic ozonation rather than adsorption alone, the phenol adsorption capacity of the FMM catalysts was evaluated (Figure S2): the phenol concentration remained essentially unchanged over 30 min; together with the low BET surface areas listed in Table S2 (0.6, 1.5, and 2.8 m^2 g^{-1} for FM, 0.08FMM, and 0.12FMM, respectively), this confirms that adsorption contributes negligibly to pollutant removal. The superior removal performance of 0.08FMM can therefore be attributed to its excellent

catalytic ozonation activity. Optimization of the key electrodeposition parameters (current and total time) and the corresponding optimal conditions are provided in Figure S3. Under the optimal conditions identified by this screening (±180 mA alternating current with a total deposition time of 9000 s), 0.08FMM reached a maximum phenol removal of 87.8% (Figure S3); this is the value referenced in the Abstract and Conclusions. Under the same optimized catalytic conditions, TOC removal reached 60.5% after 30 min (Table S3), higher than the 51.4% preliminary-condition value but still substantially below phenol removal, confirming incomplete mineralization and persistence of partially oxidized intermediates. All 0.08FMM samples used in the stability, XPS, and mechanistic studies below were prepared under these optimized conditions.

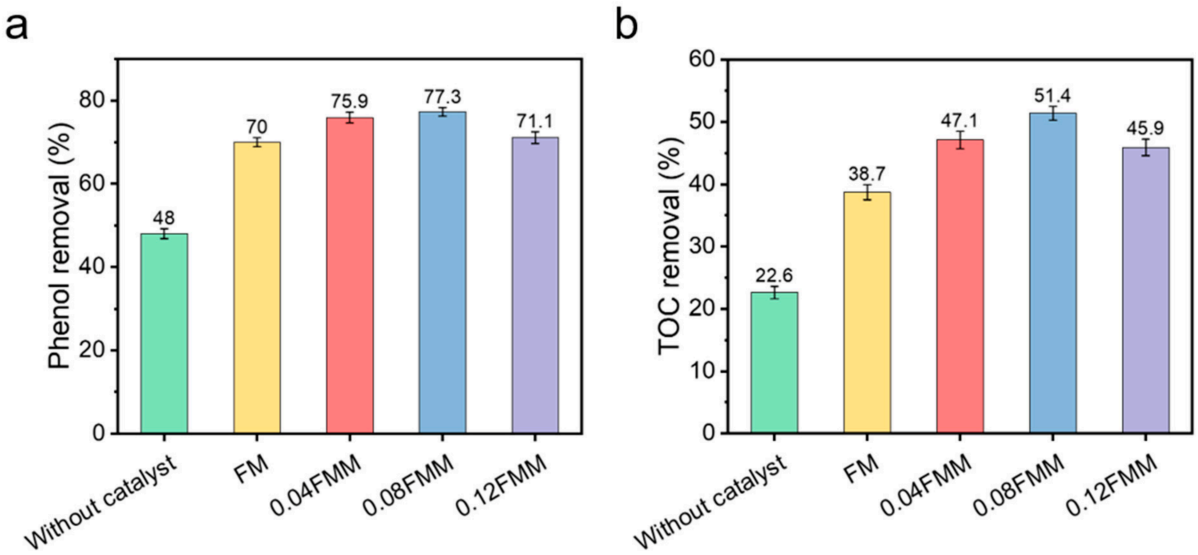


Figure 1. (**a**) Phenol removal and (**b**) TOC removal over different catalysts after 30 min of reaction (preliminary electrodeposition conditions: ±240 mA, 300 cycles, 30 s per cycle). Data are mean ± SD from three independent measurements (n = 3).

In catalytic ozonation, high stability and low metal leaching are essential for efficient and safe long-term operation. The short-term cycling stability of 0.08FMM was evaluated through five consecutive reaction cycles (Figure 2). Phenol removal was 87.7% in the first cycle, decreased to 83% in the second cycle, and was maintained at 81%, 80%, and 79% over the subsequent three cycles; the corresponding dissolved Fe concentrations in the effluent were 18.6, 11.4, 8.3, 7.5, and 5.7 μg L^{-1}, and this low and progressively decreasing leaching is consistent with the gradual washout of weakly bound surface species, after which the more strongly anchored core sustains catalytic activity. The largest activity loss occurred between the first and second cycles, whereas the subsequent changes were smaller, consistent with an initial adjustment of the outer surface layer. Because Mn leaching was not quantified in this five-cycle dataset, the activity loss cannot be assigned to Fe leaching alone; loss of weakly bound Fe/Mn species and/or surface restructuring remain possible contributors. This monotonic decrease is mechanistically informative: Fe leaching in impregnated or hydrothermally grown iron catalysts typically persists or even accelerates across cycles as the bubble-induced shear continues to strip loosely bound species, whereas the electrochemically anchored layer here appears to undergo an initial self-passivation, with the remaining surface being progressively enriched in strongly adhered active species. Accordingly, the five-cycle test is best described as moderate short-term cycling stability with an initial conditioning/self-passivation stage. To evaluate extended continuous operation, a 20 h time-on-stream test was performed under the optimized conditions (Figure S5). Phenol removal decreased from approximately 87.7% at the beginning of

the test to ~82% during the first 2 h and then remained near 79–80% through 20 h. Over the same period, Fe leaching decreased from ~18.6 to ~4–5 μg L^{-1}, while Mn leaching decreased from ~5–6 to ~1–2 μg L^{-1}. The declining leaching concentrations and subsequent activity plateau are consistent with initial removal of weakly bound Fe/Mn-containing species followed by retention of a more strongly anchored catalytic layer, although atomic-scale surface restructuring is not directly resolved. The robustness of 0.08FMM was further tested across a wide pH window (4.0–11.0). As shown in Figure S4, the catalytic ozonation performance was almost insensitive to the initial pH of the phenol solution, indicating that 0.08FMM can operate effectively in both acidic and alkaline environments. Whereas iron-based catalysts often exhibit pH-dependent activity owing to changes in the protonation state of surface Fe–OH groups and limited Fe^{3+}/Fe^{2+} regeneration kinetics, the origin of the pH-insensitivity observed here cannot be fully resolved from the present data. Possible contributions include the Fe–Mn electronic interaction discussed in Section 2.3 and the abundant surface hydroxyl sites identified by O 1s XPS (Section 2.3) and supported by the radical-quenching experiments (Section 2.4), which together may buffer the catalytic cycle against changes in the bulk solution pH.

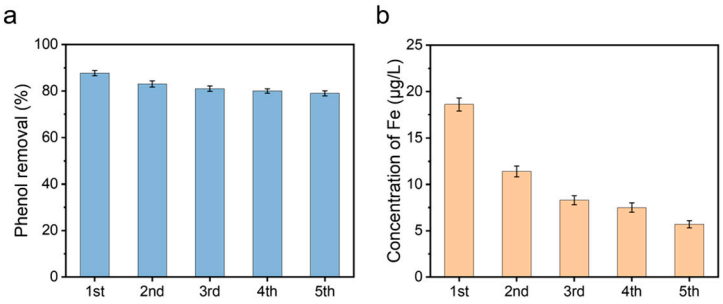


Figure 2. (**a**) Phenol removal and (**b**) Fe-leaching concentration in the effluent over 0.08FMM during five consecutive short-term reaction cycles (each cycle: 30 min, fresh phenol feed, optimised electrodeposition conditions). Data are mean ± SD from three independent measurements (n = 3).

2.2. Morphology and Bulk Structure of the Catalysts

The morphologies of the FMM and FM catalysts were examined by SEM (Figure 3). The FM catalyst exhibited an irregular flake-like surface with a relatively rough and discrete morphology, whereas 0.08FMM displayed fine and uniform granular aggregates with similar particle sizes and a closely packed, well-ordered microstructure, favourable for exposing additional surface hydroxyl active sites. The BET surface area of 0.08FMM (1.5 m^2 g^{-1}, Table S2) is intermediate between FM and 0.12FMM. In contrast, 0.12FMM showed significantly more pronounced particle aggregation: the aggregate size became larger and the distribution was looser, indicating that Mn doping strongly modifies the surface microstructure of the iron-mesh catalyst. It is worth noting that 0.12FMM exhibits the largest BET surface area (2.8 m^2 g^{-1}) yet does not show the highest activity, indicating that total BET surface area is not the dominant descriptor of catalytic performance for this system; rather, the density of accessible surface hydroxyl groups ($–OH_{lat}$, quantified in Section 2.3) appears to be the more relevant active-site measure. The EDS elemental mapping of 0.08FMM (Figure 3d) showed that Fe is distributed uniformly along the mesh structure as the dominant component of the substrate; O is uniformly dispersed and mainly originates from the surface oxide layer or adsorbed oxygen species; Mn, although present at a relatively low overall content, is also uniformly distributed across the surface, confirming that Mn was successfully incorporated into the iron-mesh framework [22].

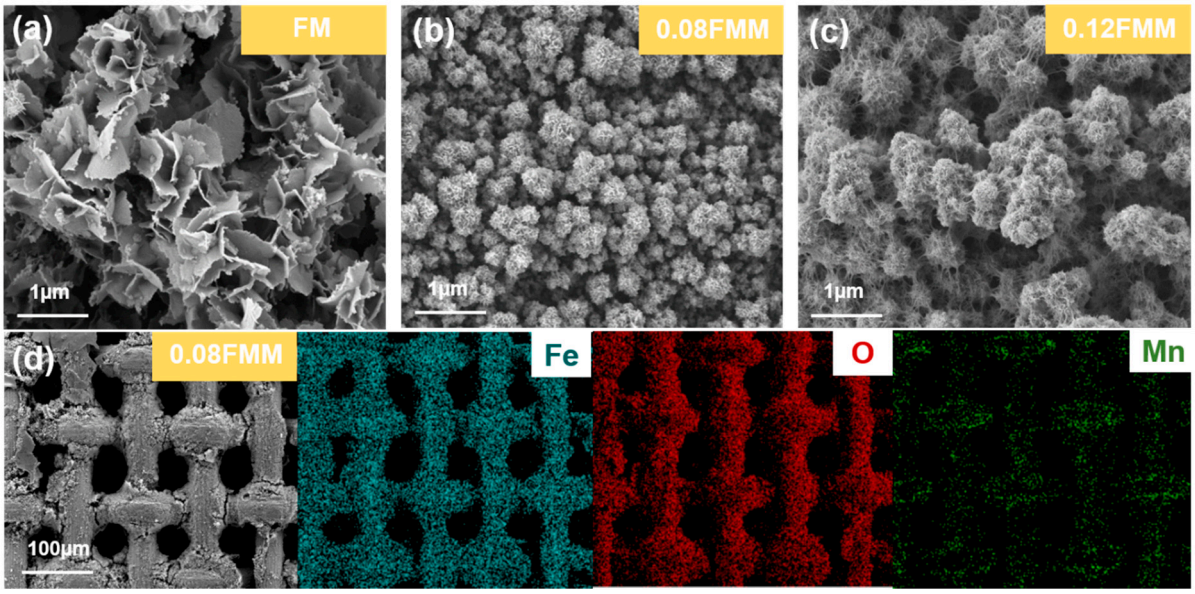


Figure 3. SEM images of (**a**) FM, (**b**) 0.08FMM, and (**c**) 0.12FMM; (**d**) EDS elemental mapping of 0.08FMM.

The bulk crystalline structures of FM, 0.08FMM, and 0.12FMM before and after reaction were analyzed by XRD (Figure 4). For the fresh (pre-reaction) FM and FMM catalysts, diffraction peaks of Fe (2θ = 44.8°, 65.2°), Fe_2O_3 (2θ = 35.8°, 62.9°), and FeO(OH) (2θ = 21.3°, 26.8°) were observed. The characteristic Fe peaks originate from the metallic mesh, and FeO(OH) and Fe_2O_3 likely formed through dehydration of $Fe(OH)_3$ during drying. The Fe_2O_3 peaks of 0.08FMM are very weak, indicating poor crystallinity. No new phases were detected in 0.08FMM or 0.12FMM upon Mn doping, suggesting that Mn does not form an independent crystalline phase but is instead highly dispersed within the iron-based framework. The enlarged XRD region shows that, relative to FM, the Fe_2O_3 peak (35.8°) shifts to lower angles by 0.09° for 0.08FMM and 0.03° for 0.12FMM, which can be rationally ascribed to the incorporation of larger-radius Mn ions into the Fe_2O_3 lattice to form a solid solution; the larger shift for 0.08FMM is consistent with its higher actual Mn content (14.24 wt%) compared with 0.12FMM (11.28 wt%) measured by ICP-OES (Table S1), confirming that the lattice perturbation tracks the true Mn loading rather than the nominal electrolyte concentration [23]. After reaction, the peak positions of all phases are essentially unchanged, indicating that the main phases remain stable during the catalytic process; the peak-shift trend of the Fe_2O_3 (35.8°) reflection for 0.08FMM and 0.12FMM is consistent with that of the fresh samples. Using the Scherrer equation for the $2\theta \approx 35.8°$ Fe_2O_3 reflection, the apparent Fe_2O_3 crystallite size of the post-reaction samples follows the order FM (14.4 nm) > 0.12FMM (12.4 nm) > 0.08FMM (5.5 nm), indicating an inverse correlation between the actual Mn loading (Table S1) and the degree of Fe_2O_3 aggregation. The values listed above represent apparent crystallite sizes derived from the Scherrer equation; possible contributions from microstrain and lattice defects were not deconvoluted, and the values for the weakly crystalline 0.08FMM should therefore be regarded as semi-quantitative estimates. A Williamson–Hall analysis was not performed because the weak and partially overlapping Fe_2O_3 reflections, particularly for 0.08FMM, do not provide sufficient independent peaks for a robust linear fit.

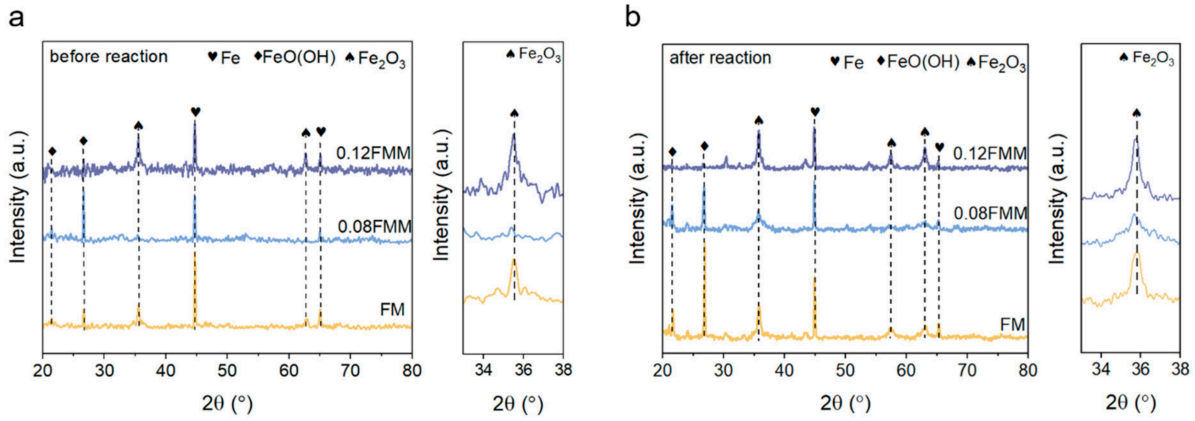


Figure 4. XRD patterns of FM, 0.08FMM, and 0.12FMM catalysts (**a**) before and (**b**) after reaction.

2.3. Surface Electronic Structure of the Catalysts

The chemical composition and surface electronic structure of the iron-mesh catalysts were analyzed by quasi in situ XPS. Figure 5a,b show the Fe 2p spectra of FM and FMM catalysts: the $2p_{3/2}$ and $2p_{1/2}$ peaks at 710.7–710.9 eV/724.5–724.6 eV and 713.1–713.3 eV/727.4–727.6 eV are assigned to Fe^{2+} and Fe^{3+}, respectively [22]. Mn is also present in multiple oxidation states (Figure 5c,d), with peaks at 641.0, 642.1, and 643.2–643.4 eV corresponding to Mn^{2+}, Mn^{3+}, and Mn^{4+}, respectively [16]. The Fe and Mn compositions before and after reaction differ: the Fe^{2+} fraction of 0.08FMM increased from 52.63% to 62.89% and that of 0.12FMM increased from 57.80% to 60.98% after reaction, whereas the Fe^{2+} fraction of FM decreased from 60.24% to 50.76%. Given the very different phenol-removal behaviors of FMM and FM, it is reasonable to infer that Fe^{2+} promotes the catalytic activation of ozone and that the poor activity of FM originates from the pronounced decrease in Fe^{2+}; therefore, regeneration of Fe^{2+} is the key factor that sustains the high activity of the FMM catalysts. The post-reaction Mn^{2+} fraction decreased noticeably (from 43.51% to 32.84% for 0.08FMM and from 41.97% to 34.12% for 0.12FMM, Figure 5c,d), with concurrent increases in Mn^{3+} and Mn^{4+}. Taken together with the Fe^{2+} trend above, these observations support the conclusion that the Fe–Mn interaction drives an electron-transfer process that enhances catalytic ozonation activity. Two caveats to this interpretation deserve explicit discussion. First, an alternative explanation of the Fe^{2+} rise—preferential surface dissolution of Fe^{3+} producing an apparent shift in the Fe^{2+}/Fe^{3+} ratio sampled by XPS (which probes only the top ~3 nm) rather than genuine in situ reduction—cannot be fully excluded on the basis of XPS data alone. However, two observations argue against preferential Fe^{3+} dissolution as the dominant driver: (i) the effluent Fe concentration decreases monotonically across cycles (18.6 → 5.7 μg L^{-1}, Figure 2b), indicating shrinking rather than sustained Fe loss; (ii) FM shows the opposite trend (Fe^{2+} fraction decreases after reaction), which would be difficult to reconcile with a purely leaching-driven origin. We note that direct one-electron transfer from Mn^{2+} to Fe^{3+} in aqueous solution is thermodynamically unfavourable ($E^{\circ}(Mn^{3+}/Mn^{2+})$ = +1.51 V vs. $E^{\circ}(Fe^{3+}/Fe^{2+})$ = +0.77 V). The XPS trends observed here are therefore most plausibly mediated by ozone-derived intermediates (e.g., $Mn^{2+} + O_3 \rightarrow Mn^{3+} + \cdot O_2^-$; followed by $\cdot O_2^-$ reducing Fe^{3+} at the surface) or via Mn–O–Fe bridging-bond electron exchange, rather than by free aqueous-ion redox; the present XPS data alone cannot distinguish these mechanistic alternatives.

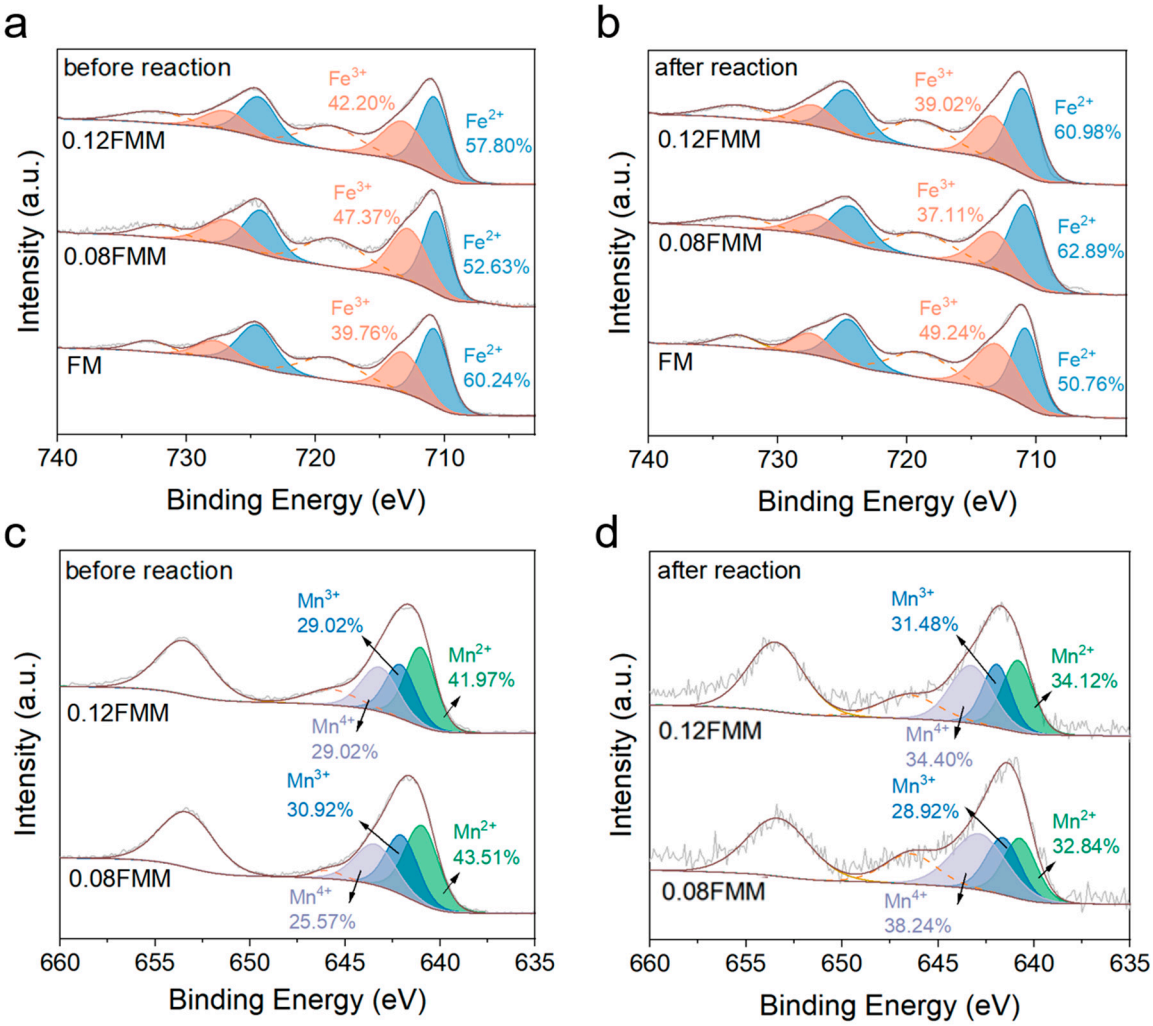


Figure 5. Quasi in situ XPS spectra of FM and FMM catalysts before and after reaction. Fe 2p region (**a**) before and (**b**) after reaction. Mn 2p region (**c**) before and (**d**) after reaction.

The O 1s spectra of the FM and FMM catalysts are shown in Figure 6. Three fitted peaks at 529.7–530.0, 531.1–531.5, and 533.1–533.2 eV are tentatively assigned to lattice oxygen ($–O_{lat}$), lattice hydroxyl groups ($–OH_{lat}$), and adsorbed hydroxyl groups ($–OH_{ads}$), respectively [24]; the 531 eV peak has also been attributed to surface-bound hydroxyls or oxygen vacancies in some studies, and our argument below relies on the post-reaction depletion trend rather than on the exact molecular identity. The $–OH_{lat}$ groups are rich in surface –OH, which can react with ozone through redox reactions to generate ROS [24,25]. Among the fresh catalysts, 0.08FMM has the highest fraction of $–OH_{lat}$ (62.1%), indicating the most abundant surface –OH. The $–OH_{lat}$ fraction decreases in all catalysts after reaction, consistent with participation of $–OH_{lat}$ in the catalytic pathway. The absolute decreases in the $–OH_{lat}$ fraction for 0.08FMM, 0.12FMM, and FM are 21.8, 16.1, and 2.4 percentage points, respectively (Figure 6a vs. Figure 6b), indicating that Mn doping greatly enhances the involvement of surface –OH in the catalytic reaction. The order of decrease (0.08FMM > 0.12FMM > FM) is consistent with the order of catalytic activity, further supporting the conclusion that surface –OH on FMM catalysts is strongly correlated with the catalytic activity and supporting a role for surface –OH as a principal active-site-related species (a quantitative structure–activity correlation with more compositional points would be needed to support a stricter causal claim). This interpretation is further supported by the radical-quenching experiments in Section 2.4, in which the addition of Na_3PO_4 (a

surface-hydroxyl blocker) markedly suppresses phenol removal. Complementary ATR-FTIR measurements (Figure S6) showed that, after normalization to the metal–oxygen region, the integrated 3000–3700 cm^{-1} O–H envelope decreased by approximately 28% for 0.08FMM after reaction, compared with approximately 8% for FM. The H–O–H bending region near 1630 cm^{-1} showed a smaller change, while the principal metal–oxygen bands in the 450–750 cm^{-1} region remained comparatively stable. Because adsorbed molecular water also contributes to the broad O–H envelope, the FTIR result is treated as complementary evidence for changes in hydroxyl/water-related surface species rather than a species-exclusive assignment.

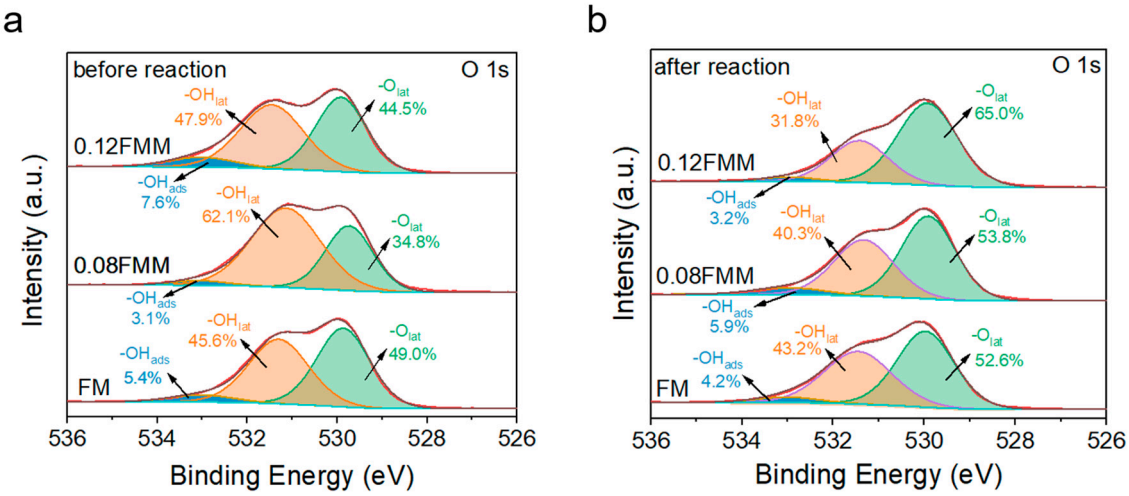


Figure 6. Quasi in situ XPS O 1s spectra of FM, 0.08FMM, and 0.12FMM catalysts (**a**) before and (**b**) after reaction, with peak assignments to lattice oxygen ($–O_{lat}$), surface hydroxyl groups ($–OH_{lat}$), and adsorbed hydroxyl/molecular water ($–OH_{ads}$).

2.4. Reaction Mechanism

The interaction between ozone (or the organic pollutant) and the catalyst has been reported to be the dominant pathway in catalytic ozonation [1]. As shown above, the contributions of adsorption on FM and FMM catalysts are negligible; accordingly, the main mechanism is proposed to involve the interaction of ozone with the iron-mesh catalyst, which produces radicals that oxidize the organic pollutant. To verify this hypothesis, the ozone-decomposition behavior in a saturated ozone aqueous solution (in the absence of phenol) was monitored over different catalysts (Figure 7a). The 0.08FMM catalyst significantly accelerated ozone decomposition: at 5 min, 75% of ozone had decomposed in the 0.08FMM system and 61% had decomposed over FM, compared with only 17.7% in the ozone-only system. At 30 min, 40.5% of ozone remained in the ozone-only system, whereas 94% of ozone had decomposed over 0.08FMM and 84% over FM. The ozone-decomposition rate in the catalytic systems correlates with the phenol-removal efficiency, supporting the conclusion that the interaction of 0.08FMM with ozone accelerates ozone decomposition and contributes importantly to efficient phenol removal in the catalytic ozonation system.

During ozone decomposition, reactive radicals such as HO· (oxidation potential ≈ 2.8 eV) are generated; these radicals have a low oxidation barrier toward organic compounds and can markedly improve oxidation efficiency [26]. Radical-quenching experiments were performed to identify the active species (Figure 7b). When TBA was added as a HO· scavenger [27], phenol removal was substantially suppressed, supporting HO· generation during the catalytic reaction between ozone and FMM and an important role for HO· in phenol degradation. Na_3PO_4 can bind to surface hydroxyl groups and suppress HO· formation [28]; the decrease in removal upon Na_3PO_4 addition therefore further corroborates the role of surface hydroxyl groups as active sites. p-BQ was used as an $\cdot O_2^-$

scavenger [29]; its addition also reduced phenol removal, consistent with a contribution from $\cdot O_2^-$ to phenol degradation. It should be noted, however, that $\cdot O_2^-$ has a pK_a of ~4.8 and therefore coexists with its protonated form $HO_2\cdot$ under the near-neutral conditions used here, with a lifetime on the order of microseconds and facile disproportionation to H_2O_2 (which can in turn yield HO·). The suppression observed upon p-BQ addition may therefore partly reflect the quenching of downstream species (H_2O_2 or the HO· generated from its decomposition) rather than direct scavenging of $\cdot O_2^-$. This caveat does not overturn the radical-pathway conclusion but bounds how strongly the p-BQ signal can be used to argue for a free-solution $\cdot O_2^-$ role. A semi-quantitative deconvolution of the HO· and $\cdot O_2^-$ contributions can be constructed from Figure 7b by assuming approximately additive, independently acting quenching: the HO·-specific contribution to phenol removal is then ~ ($R_0 - R_{TBA}$), and the $\cdot O_2^-$-specific contribution ~ ($R_0 - R_{p\text{-}BQ}$), where R_0 is the phenol removal without quencher. Applied to the 0.08FMM data in Figure 7b (R_0 = 87.8%, $R_{TBA} \approx 54\%$, $R_{p\text{-}BQ} \approx 47\%$, $R_{Na3PO4} \approx 71\%$), the apparent upper bounds on the HO·-specific and $\cdot O_2^-$-specific contributions are ~34 and ~41 percentage points, respectively, and the ~17 percentage-point drop upon Na_3PO_4 addition reflects partial blocking of the surface –OH sites that serve as the source of HO·, and so should not be regarded as an independent third contribution but rather as complementary evidence for the mechanistic role of surface hydroxyls identified by O 1s XPS in Section 2.3. The sum of these apparent upper bounds (~75 pp) exceeds the total catalytic increment over ozone alone (87.8 − 48 = ~40 pp), which directly demonstrates that the two pathways share common intermediates rather than acting independently—most plausibly via the $Mn^{2+} + O_3 \rightarrow \cdot O_2^- \rightarrow H_2O_2 \rightarrow$ HO· chain implied by the pK_a discussion above. The ozone-only system itself shows only small scavenger effects (~9 pp drop with p-BQ and ~3 pp with TBA), and if these are subtracted as an approximate baseline—recognising that the true scavenger effect in the catalysed system may differ because most phenol is then oxidised by radicals rather than by O_3 directly—the catalyst-specific HO· and $\cdot O_2^-$ contributions become comparable in magnitude (~30 pp each). The qualitative conclusion is therefore that HO· and $\cdot O_2^-$ contribute comparably to phenol oxidation, with neither species alone accounting for the catalytic enhancement. As a control, TBA and p-BQ had only a limited effect on phenol removal in the absence of catalyst, indicating that in the presence of FMM, the contribution of ozone self-decomposition to the overall oxidation is negligible. It is acknowledged that none of these chemical scavengers is perfectly selective: TBA also reacts with surface-bound HO·; p-BQ can be directly oxidized by O_3 and may compete with phenol for ozone consumption; and Na_3PO_4 can simultaneously block surface –OH sites and modify the ionic strength of the solution. The quenching results presented here therefore provide internally consistent but not unambiguous evidence for the proposed radical pathway.

To provide a more direct probe of radical formation, DMPO spin-trapping EPR measurements were performed (Figure S7). The 0.08FMM + O_3 system exhibited the strongest characteristic four-line DMPO–OH signal with an approximate 1:2:2:1 intensity pattern; O_3 alone gave a weak signal and FM + O_3 an intermediate signal. With the integrated DMPO–OH signal of 0.08FMM + O_3 normalized to 1.00, the corresponding intensities were ~0.18 for O_3 alone, ~0.50 for FM + O_3, and ~0.21 for 0.08FMM + O_3 + TBA. The strong enhancement over 0.08FMM and suppression by TBA directly support HO· generation, while the EPR result does not by itself uniquely define every elementary surface reaction step.

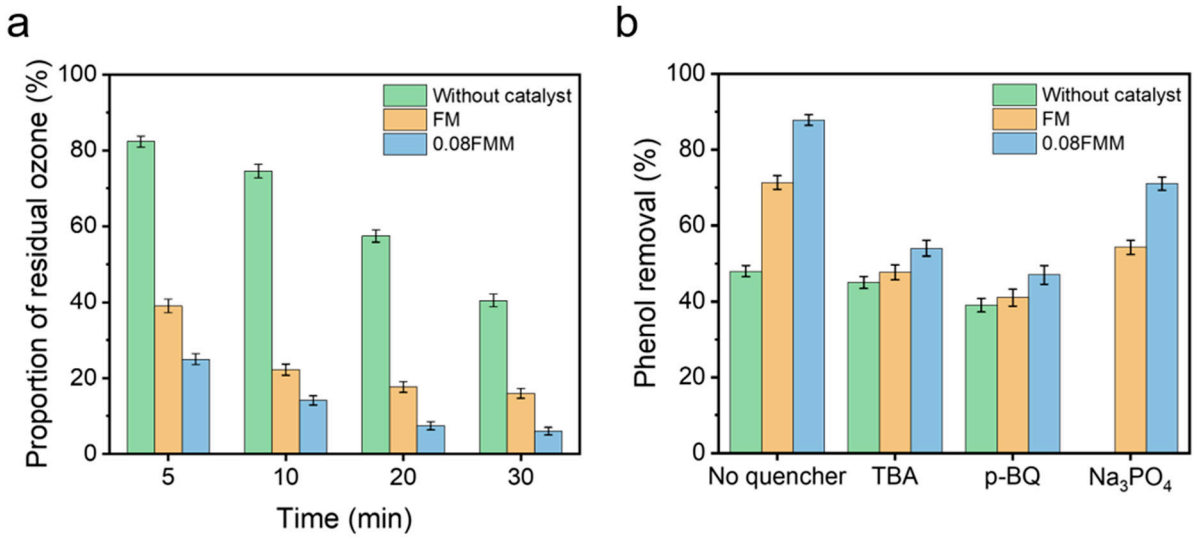


Figure 7. (**a**) Residual ozone fraction during O_3 decomposition over without-catalyst, FM, and 0.08FMM systems (saturated O_3 aqueous solution, no phenol). (**b**) Phenol removal over without-catalyst, FM, and 0.08FMM in the absence of quencher and with TBA, p-BQ, or Na_3PO_4 added. Data are mean ± SD from three independent measurements (n = 3).

3. Materials and Methods

3.1. Catalyst Preparation

Commercial iron mesh (100 mesh, purity > 99.9%, Anping Chulin Metal Co., Ltd., Hengshui, China) was used as the substrate, and Fe–Mn and bare Fe mesh catalysts were prepared by a modified cyclic chronopotentiometry method. The iron mesh was first ultrasonically cleaned in ethanol and ultrapure water for 10 min each. Then, 1.432, 2.863, and 4.295 g of 50 wt% $Mn(NO_3)_2$ solution and 0.680 g of $NaNO_3$ were dissolved separately in 100 mL of deionized water and ultrasonicated to give transparent, homogeneous $Mn(NO_3)_2$ solutions (0.04, 0.08, and 0.12 mol L^{-1}) and a 0.08 mol L^{-1} $NaNO_3$ solution. The $Mn(NO_3)_2$ electrolytes were used without any supporting electrolyte; $NaNO_3$ served only as the sole electrolyte for preparing the bare FM catalyst. Two pieces of iron mesh and the corresponding nitrate solution were placed in an electrolytic cell and treated using an electrochemical workstation (CORRTEST CS310X, Wuhan Corrtest Instruments Corp., Ltd., Wuhan, China). For the preliminary composition screening shown in Figure 1, an alternating current of ±240 mA was applied for 300 cycles (30 s per cycle; 9000 s total). The electrodeposition current and total treatment time were subsequently optimized (Figure S3); the optimized condition used for the stability, XPS, and mechanistic studies was ±180 mA for 9000 s (30 s per cycle). After electrochemical treatment, the mesh catalysts were ultrasonicated in ultrapure water for 5 min to remove any clogging material and then dried in an oven at 60 °C for 2 h. The Fe–Mn catalysts prepared from $Mn(NO_3)_2$ electrolytes are denoted as x-FMM (x = 0.04, 0.08, 0.12), where x denotes the nominal $Mn(NO_3)_2$ concentration (mol L^{-1}) in the electrodeposition electrolyte rather than the measured Mn loading; the bare iron-mesh catalyst prepared from the $NaNO_3$ electrolyte is denoted as FM. The macroscopic appearance and the elemental composition (determined by ICP-OES) of the catalysts are presented in Figure S1 and Table S1, respectively.

3.2. Catalyst Characterization

Elemental contents were determined by inductively coupled plasma–optical emission spectrometry (ICP-OES, Agilent 5800, Agilent Technologies, Santa Clara, CA, USA). XRD was performed on a Bruker D8-Advance diffractometer (Bruker AXS GmbH, Karlsruhe,

Germany) using Cu Kα radiation (λ = 0.154 nm) operated at 40 kV and 40 mA; patterns were collected over 2θ = 20–80° with a step size of 0.02°, and the apparent Fe_2O_3 crystallite size was estimated from the 2θ ≈ 35.8° reflection using the Scherrer equation. The BET specific surface area was measured on a BELSORP-MAX instrument (MicrotracBEL Corp., Osaka, Japan). SEM images were acquired on an FEI Helios G4 field-emission microscope (FEI Company, Hillsboro, OR, USA) at 2.0 kV, and EDS elemental mapping was performed on a ThermoFisher Talos F200X instrument (Thermo Fisher Scientific, Waltham, MA, USA) equipped with four in-column Super-X detectors. Quasi in situ XPS measurements were carried out on a Thermo ESCALAB 250Xi spectrometer (Thermo Fisher Scientific, Waltham, MA, USA) with a monochromatic Al Kα source (1486.6 eV; pass energy = 20.0 eV), and binding energies were calibrated using the C 1s peak (284.8 eV). To avoid air exposure, samples were transferred directly between the vacuum pretreatment chamber and the analysis chamber after reaction treatment. ATR-FTIR spectra of FM and 0.08FMM were collected before and after catalytic ozonation after identical pretreatment and drying. The spectra were background-corrected and normalized to the comparatively stable metal–oxygen vibration region before comparison.

3.3. Evaluation of Catalytic Performance

Phenol-degradation experiments were conducted at 25 °C in a jacketed up-flow fixed-bed reactor. The reaction tube was made of quartz glass with an outer diameter of 18 mm, an inner diameter of 14 mm, and a length of 30 cm; a porous quartz frit was placed at the bottom to ensure uniform dispersion of ozone bubbles, and four inward protrusions located 1 cm above the frit supported the mesh catalyst (ca. 1 g) horizontally in the reactor. Ozone was generated by a 3S-A3 ozone generator (Tonglin Hi-Tech, Beijing, China) using pure O_2 as the feed gas, with a gas flow rate of 0.2 L min^{-1}, and the ozone concentration in the O_2 feed stream (gas phase) was 30 mg L^{-1} (corresponding to a feed rate of 6 mg min^{-1}). The catalyst loading was 1 g, and a 300 mg L^{-1} phenol solution was continuously fed from the bottom of the reactor through the catalyst bed by a peristaltic pump. For safety, an ozone tail-gas absorber and alarm were installed at the end of the setup. The effluent was collected in a receiving bottle, and 0.1 mol L^{-1} $Na_2S_2O_3$ was added to quench any residual ozone. The phenol concentration was determined by HPLC (mobile phase: methanol/water = 45/55, flow rate 1 mL min^{-1}, column temperature 308 K, detection wavelength 275 nm), and total organic carbon (TOC) was measured using a Shimadzu TOC-V_{CPH} analyzer (Shimadzu Corporation, Kyoto, Japan). The phenol (or TOC) removal efficiency was calculated as:

$$\text{Removal (\%)} = (1 - C/C_0) \times 100\% \quad (1)$$

where C_0 is the initial phenol (or TOC) concentration, and C is the concentration after 30 min of reaction. Radical-quenching experiments were performed using tert-butanol (TBA) to scavenge HO·, p-benzoquinone (p-BQ) to scavenge $\cdot O_2^-$, and Na_3PO_4 to suppress the involvement of surface hydroxyl groups so as to identify the dominant reactive species in the reaction system. DMPO spin-trapping EPR measurements were conducted for O_3 alone, FM + O_3, 0.08FMM + O_3, and 0.08FMM + O_3 + TBA under otherwise identical ozonation conditions. For long-term testing, 0.08FMM was operated continuously for 20 h under the optimized conditions, with effluent sampled periodically for phenol analysis and Fe/Mn determination by ICP-OES. Unless otherwise stated, catalytic measurements were performed in triplicate and are reported as mean ± standard deviation (SD).

4. Conclusions

A Mn-doped, structured iron-mesh catalyst was successfully synthesized by a modified cyclic chronopotentiometry method, and its catalytic performance and ozone-activation

behavior in the catalytic ozonation of phenol were systematically investigated. XRD, SEM, and BET characterizations show that the incorporation of Mn reduces the Fe_2O_3 crystallite size and produces a denser, more uniform microstructure, thereby increasing the density of accessible surface hydroxyl active sites. Quasi in situ XPS, DMPO-EPR, ATR-FTIR, ozone-decomposition, and radical-quenching measurements jointly support a radical-mediated pathway in which hydroxyl/water-related surface species participate in ozone activation and HO· generation, while Fe–Mn interactions are consistent with facilitated Fe^{2+} regeneration across cycles. Compared with the unmodified bare iron-mesh catalyst prepared in a $NaNO_3$ electrolyte, the Fe–Mn mesh catalyst delivers higher phenol and TOC removal under the same operating conditions. In particular, 0.08FMM reaches 87.8% phenol removal and 60.5% TOC removal after 30 min at 25 °C under optimised electrodeposition conditions. In a 20 h continuous-flow test, phenol removal decreases during the initial ~2 h and then stabilizes near 79–80%, while Fe and Mn leaching decline to ~4–5 and ~1–2 μg L^{-1}, respectively, by 20 h, indicating moderate extended-operation stability after an initial conditioning period. The single electrochemical anchoring-step strategy therefore provides a route for preparing structured heterogeneous catalysts that integrates active-site abundance with mechanical robustness.

Supplementary Materials: The following supporting information can be downloaded at: https://www.mdpi.com/article/10.3390/catal16100926/s1, Figure S1: Photographs of (a) FM, (b) 0.04FMM, (c) 0.08FMM, and (d) 0.12FMM after electrochemical deposition and drying at 60 °C for 2 h, photographed under ambient laboratory lighting against a white background. Each mesh sample is approximately 6 × 4 cm; Table S1: Mn and Fe contents of *x*-FMM catalysts; Figure S2: Adsorption of phenol by FM and FMM catalysts; Table S2: BET specific surface areas of FM and FMM catalysts; Figure S3: Effects of (a) current and (b) total time during electrodeposition on the catalytic ozonation performance of FMM catalysts for phenol removal. In (a) the total deposition time was fixed at 9000 s; in (b) the current was fixed at ±180 mA; in both panels each cycle was 30 s. Catalytic test conditions: [phenol]0 = 300 mg L^{-1}, O_3 feed rate = 6 mg min^{-1} (0.2 L min^{-1} pure O_2 carrying 30 mg L^{-1} O^3), catalyst loading ~1 g, 25 °C, 30 min reaction time; Figure S4: Phenol removal at initial pH of 4, 7, and 11 over 0.08FMM and in the absence of a catalyst. Initial pH was adjusted with 0.1 mol L^{-1} HCl or NaOH; no buffer was used, so the pH may drift during the 30 min reaction. Other catalytic test conditions as in Figure S3; Figure S5: (a) Phenol removal and (b) Fe and Mn leaching concentrations during 20 h continuous operation of 0.08FMM under optimized conditions; Figure S6: ATR-FTIR spectra of FM and 0.08FMM before and after catalytic ozonation; Figure S7: DMPO spin-trapping EPR spectra of the O_3-only, FM + O_3, 0.08FMM + O_3, and 0.08FMM + O_3 + TBA systems; Table S3: Phenol and TOC removal over 0.08FMM under preliminary and optimized electrodeposition conditions. Refs. [30,31] are cited in Supplementary Materials.

Author Contributions: Conceptualization, F.S. and H.G.; investigation, F.S. and J.W.; writing—original draft preparation, F.S.; writing—review and editing, H.G. and M.Z.; project administration, J.X.; resources, M.Z. All authors have read and agreed to the published version of the manuscript.

Funding: This research was funded by the National Natural Science Foundation of China, grant numbers 22578125 and 22078089; the Shanghai Pilot Program for Basic Research, grant number 22TQ1400100-7; the Basic Research Program of Science and Technology Commission of Shanghai Municipality, grant number 22JC1400600; and the Fundamental Research Funds for the Central Universities.

Data Availability Statement: The data presented in this study are available from the corresponding author upon reasonable request.

Conflicts of Interest: The authors declare no conflict of interest.

References

1. Ren, T.; Ouyang, C.; Zhou, Z.; Chen, S.; Yin, M.; Huang, X.; Zhang, X. Mn-doped carbon-Al_2SiO_5 fibers enable catalytic ozonation for wastewater treatment: Interface modulation and mass transfer enhancement. *J. Hazard. Mater.* **2023**, *460*, 132307. [CrossRef] [PubMed]
2. Forzatti, P.; Ballardini, D.; Sighicelli, L. Preparation and characterization of extruded monolithic ceramic catalysts. *Catal. Today* **1998**, *41*, 87–94. [CrossRef]
3. Govender, S.; Friedrich, H.B. Monoliths: A Review of the Basics, Preparation Methods and Their Relevance to Oxidation. *Catalysts* **2017**, *7*, 62. [CrossRef]
4. Wang, A.; Guan, J.; Zhang, L.; Wang, H.; Ma, G.; Fan, G.; Tang, W.; Han, N.; Chen, Y. In Situ Synthesis of Monolithic Cu_2O–CuO/Cu Catalysts for Effective Ozone Decomposition. *J. Phys. Chem. C* **2022**, *126*, 317–325. [CrossRef]
5. Shukla, P.; Wang, S.; Sun, H.; Ang, H.-M.; Tadé, M. Adsorption and heterogeneous advanced oxidation of phenolic contaminants using Fe loaded mesoporous SBA-15 and H_2O_2. *Chem. Eng. J.* **2010**, *164*, 255–260. [CrossRef]
6. Yang, X.-J.; Xu, X.-M.; Xu, J.; Han, Y.-F. Iron Oxychloride (FeOCl): An Efficient Fenton-Like Catalyst for Producing Hydroxyl Radicals in Degradation of Organic Contaminants. *J. Am. Chem. Soc.* **2013**, *135*, 16058–16061. [CrossRef] [PubMed]
7. Ahmadi, M.; Kakavandi, B.; Jaafarzadeh, N.; Akbar Babaei, A. Catalytic ozonation of high saline petrochemical wastewater using PAC@$FeIIFe_2IIIO_4$: Optimization, mechanisms and biodegradability studies. *Sep. Purif. Technol.* **2017**, *177*, 293–303. [CrossRef]
8. Du, X.; Li, C.; Zhao, L.; Zhang, J.; Gao, L.; Sheng, J.; Yi, Y.; Chen, J.; Zeng, G. Promotional removal of HCHO from simulated flue gas over Mn-Fe oxides modified activated coke. *Appl. Catal. B Environ.* **2018**, *232*, 37–48. [CrossRef]
9. Zhang, J.; Zhang, X.; Wang, Y. Degradation of phenol by a heterogeneous photo-Fenton process using Fe/Cu/Al catalysts. *RSC Adv.* **2016**, *6*, 13168–13176. [CrossRef]
10. Xing, S.; Lu, X.; Liu, J.; Zhu, L.; Ma, Z.; Wu, Y. Catalytic ozonation of sulfosalicylic acid over manganese oxide supported on mesoporous ceria. *Chemosphere* **2016**, *144*, 7–12. [CrossRef] [PubMed]
11. Cai, S.; Liu, J.; Zha, K.; Li, H.; Shi, L.; Zhang, D. A general strategy for the in situ decoration of porous Mn–Co bi-metal oxides on metal mesh/foam for high performance de-NOx monolith catalysts. *Nanoscale* **2017**, *9*, 5648–5657. [CrossRef] [PubMed]
12. Liao, H.; Zuo, P.; Liu, M. Study on the correlation between the surface active species of Pd/cordierite monolithic catalyst and its catalytic activity. *Mater. Sci. Eng. B* **2016**, *211*, 45–52. [CrossRef]
13. Liu, Q.; Wu, H.; Gu, H.; Jiang, Z.; Zhang, W.; Li, H.; Wang, Z.; Liu, P.; Li, D.; Zhu, M. Electrochemical Synthesis of Copper Mesh-Supported Thermo-Catalysts. *Small* **2024**, *20*, 2307859. [CrossRef] [PubMed]
14. Verlato, E.; Barison, S.; Cimino, S.; Lisi, L.; Mancino, G.; Musiani, M.; Paolucci, F. Electrochemical preparation of nanostructured CeO_2-Pt catalysts on Fe-Cr-Al alloy foams for the low-temperature combustion of methanol. *Chem. Eng. J.* **2017**, *317*, 551–560. [CrossRef]
15. Ho, P.H.; Ambrosetti, M.; Groppi, G.; Tronconi, E.; Jaroszewicz, J.; Ospitali, F.; Rodríguez-Castellón, E.; Fornasari, G.; Vaccari, A.; Benito, P. One-step electrodeposition of Pd–CeO_2 on high pore density foams for environmental catalytic processes. *Catal. Sci. Technol.* **2018**, *8*, 4678–4689. [CrossRef]
16. Liu, Q.; Wu, H.; Gu, H.; Qiang, Y.; He, J.; Dong, S.; Li, D.; Jiang, Z.; Zhu, M. Electrochemical synthesized copper mesh catalysts for catalytic combustion: A comprehensive study of Mn doping and atmospheric conditions during calcination. *Chem. Eng. Sci.* **2025**, *302*, 120911. [CrossRef]
17. East China University of Science and Technology. Iron-Based Monolithic Mesh Catalyst and Preparation Method Thereof. CN121755204A, 31 March 2026.
18. Wu, H.; Han, X.; Guo, X.; Wen, Y.; Zheng, B.; Liu, B. $MnFe_2O_4/MoS_2$ catalyst used for ozonation: Optimization and mechanism analysis of phenolic wastewater treatment. *Environ. Sci. Pollut. Res.* **2024**, *31*, 45588–45601. [CrossRef] [PubMed]
19. Dai, M.; Yang, C.; Yang, L.; Lin, Y.; He, S.; Li, X.; Niu, Q.; Wu, S. Performances and mechanisms of catalytic ozonation for paint wastewater via catalysts of Fe-Mn deposited within graphitized beads of γ-Al_2O_3. *J. Clean. Prod.* **2025**, *495*, 145099. [CrossRef]
20. He, C.; Zhang, Z.; Wang, J.; Zhang, C.; Wang, S.; Zhang, K.; Wang, L.; Han, J.; Gong, C.; Li, K. Mn–Ce Bicenter of a Dual Single-Atom Catalyst Synergistically Triggers Reactive Oxygen Species Generation for Efficient Ozonation of Emerging Contaminants. *ACS ES&T Eng.* **2024**, *4*, 2002–2014. [CrossRef]
21. Song, Z.; Xu, J.; Zhang, L.; He, C.; Westerhoff, P.; Yang, X. Tailoring bidirectional electronic transfer interaction tunnels triggers sustainable and high activity of ozone catalysis for water purification. *Nat. Commun.* **2025**, *16*, 8121. [CrossRef] [PubMed]
22. Zhang, X.; Gao, R.; Li, D.; Guo, Z.; Xie, X.; Li, M.; Wei, J. Synergies of Mn modified Fe-based MOF enhanced catalytic ozonation: Charge transfer and multiple sites mechanism. *Sep. Purif. Technol.* **2024**, *343*, 127039. [CrossRef]
23. Prakash, T.; Ranjith Kumar, E.; Sumithra, M.G.; Alkhamis, K.; Munshi, A.M.; Mersal, G.A.M.; Shaaban, F.; El-Metwaly, N.M. Investigations of Structural, Morphological, Optical and Antimicrobial Behaviour of Bi Doped CdO Nanostructures. *J. Inorg. Organomet. Polym. Mater.* **2022**, *32*, 280–288. [CrossRef]
24. Xu, L.; He, Z.; Wei, X.; Shang, Y.; Shi, J.; Jin, X.; Bai, X.; Shi, X.; Jin, P. Facile-prepared Fe/Mn co-doped biochar is an efficient catalyst for mediating the degradation of aqueous ibuprofen via catalytic ozonation. *Chem. Eng. J.* **2023**, *461*, 142028. [CrossRef]

25. Yu, G.; Wang, Y.; Cao, H.; Zhao, H.; Xie, Y. Reactive Oxygen Species and Catalytic Active Sites in Heterogeneous Catalytic Ozonation for Water Purification. *Environ. Sci. Technol.* **2020**, *54*, 5931–5946. [CrossRef] [PubMed]
26. Zhang, M.; Yin, D.; Guo, J.; Wu, H.; Gong, M.; Feng, X. Ternary catalyst Mn-Fe-Ce/Al_2O_3 for the ozonation of phenol pollutant: Performance and mechanism. *Environ. Sci. Pollut. Res.* **2021**, *28*, 32921–32932. [CrossRef] [PubMed]
27. Guo, D.; Liu, Y.; Ji, H.; Wang, C.-C.; Chen, B.; Shen, C.; Li, F.; Wang, Y.; Lu, P.; Liu, W. Silicate-Enhanced Heterogeneous Flow-Through Electro-Fenton System Using Iron Oxides under Nanoconfinement. *Environ. Sci. Technol.* **2021**, *55*, 4045–4053. [CrossRef] [PubMed]
28. Sui, M.; Sheng, L.; Lu, K.; Tian, F. FeOOH catalytic ozonation of oxalic acid and the effect of phosphate binding on its catalytic activity. *Appl. Catal. B Environ.* **2010**, *96*, 94–100. [CrossRef]
29. Qi, J.; Yang, X.; Pan, P.-Y.; Huang, T.; Yang, X.; Wang, C.-C.; Liu, W. Interface Engineering of $Co(OH)_2$ Nanosheets Growing on the $KNbO_3$ Perovskite Based on Electronic Structure Modulation for Enhanced Peroxymonosulfate Activation. *Environ. Sci. Technol.* **2022**, *56*, 5200–5212. [CrossRef] [PubMed]
30. Kasprzyk-Hordern, B.; Ziółek, M.; Nawrocki, J. Catalytic ozonation and methods of enhancing molecular ozone reactions in water treatment. *Appl. Catal. B Environ.* **2003**, *46*, 639–669. [CrossRef]
31. Wang, J.; Chen, H. Catalytic ozonation for water and wastewater treatment: Recent advances and perspective. *Sci. Total Environ.* **2020**, *704*, 135249. [CrossRef] [PubMed]

Disclaimer/Publisher's Note: The statements, opinions and data contained in all publications are solely those of the individual author(s) and contributor(s) and not of MDPI and/or the editor(s). MDPI and/or the editor(s) disclaim responsibility for any injury to people or property resulting from any ideas, methods, instructions or products referred to in the content.